

# Non-equilibrium biomolecular simulation pathway analysis assisted by machine learning and graph methods

Simon Bray<sup>†,‡</sup> and Steffen Wolf<sup>\*,†</sup>

<sup>†</sup>*Biomolecular Dynamics, Institute of Physics, University of Freiburg, Freiburg, Germany*

<sup>‡</sup>*Bioinformatics Group, Institute of Informatics, University of Freiburg, Freiburg, Germany*

E-mail: [steffen.wolf@physik.uni-freiburg.de](mailto:steffen.wolf@physik.uni-freiburg.de)

Phone: +49 (0)761 203 5913. Fax: +49 (0)761 203 5883

## Abstract

Employing biased molecular dynamics simulations to enforce protein-ligand unbinding provides the path-dependent work required to effect dissociation, rather than a path-independent unbinding free energy. Analysis of such simulations therefore requires detection of paths, as well as of reaction coordinates the paths appear in. We here present two methods to identify paths and to cluster trajectories into path ensembles accordingly. The first approach is based on a contact principal component analysis for reducing the dimensionality of the input data, followed by identification of pathways and training a machine learning model for trajectory clustering. The second approach clusters trajectories according to their pairwise mean Euclidean distance employing the neighbor-net algorithm, which takes into account input data bias in the distances set and is superior to dendrogram construction. Finally, we describe a more complex case where the relevant reaction coordinate is a single intra-ligand hydrogen bond, highlighting the challenges involved in path reaction coordinate detection.

# Introduction

Simulations of time-dependent effects in biomolecular systems, such as the propagation of allosteric information<sup>1</sup> or protein-ligand complex formation and dissociation,<sup>2-4</sup> are a current focus in the fields of biomolecular simulations and non-equilibrium statistical mechanics. Understanding the time scales of the latter process for drug molecules and their target proteins is of considerable interest, as such rates have been linked to improved efficacies and reduced off-target binding of drugs.<sup>5,6</sup> Due to the time scales involved being several magnitudes outside of the capabilities of common all-atom molecular dynamics (MD) simulation methods, a range of biased simulation methods have been developed to enforce ligand unbinding and gain information on the underlying kinetics such as infrequent metadynamics,<sup>7,8</sup> random acceleration MD,<sup>9,10</sup> scaled MD<sup>11-13</sup> or weighted ensemble MD.<sup>14,15</sup> In contrast to well-established equilibrium approaches to calculate free energy  $\Delta G$  differences between bound and unbound states,<sup>16,17</sup> binding and dissociation are non-equilibrium processes. The resulting work  $W$  is thus path-dependent. Simulation methods that employ an external bias to enforce ligand (un)binding therefore need to identify

1. which trajectories take which path during unbinding, and, more fundamentally,
2. in which coordinate space the pathways occur.

In earlier publications, we developed the dissipation-corrected targeted MD (dcTMD) method<sup>18</sup> to obtain profiles of the free energy  $\Delta G$  and friction  $\Gamma$  for unbinding pathways of protein-ligand complexes<sup>19</sup> from  $W$ . These profiles can then serve as input for the numerical integration of a Langevin equation<sup>20,21</sup> to reach time scales within a biomedically relevant range of minutes and more. The dcTMD method is based on a 2<sup>nd</sup>-order cumulant expansion of the Jarzynski identity<sup>22,23</sup> and thus requires a normally distributed  $W$ . As a result, combining trajectories from different pathways together in a single analysis results in a significant overestimation of friction and a subsequent underestimation of free energies,<sup>19,24</sup> as friction corresponds to the variance of the trajectories' work profile, the second term in

the cumulant expansion.

Within the framework of non-equilibrium simulations, identifying the coordinate space of pathways is a ubiquitous problem,<sup>25-27</sup> which can be solved using methods such as contact fingerprint analysis<sup>13,28,29</sup> or, as in our case, via a principal component analysis of protein-ligand contacts (conPCA).<sup>30</sup> Choosing these two approaches already presumes that protein-ligand contacts form the relevant coordinate space in which pathways appear, which may not necessarily be the case. Identifying pathways in any coordinate space can be problematic: simple visual inspection can be tedious due to the necessity of manually inspecting hundreds of simulations.<sup>19</sup> Sorting can become ambiguous, if there is considerable overlap of trajectories from distinct pathways, which appears on shallow or rugged free energy surfaces. Additionally, the bias employed in non-equilibrium simulations can lead to artificial pseudo-stationarity, leading to artificial crossings between different pathways.<sup>19,24</sup> Commonly used dendrogram-based clustering approaches such as UPGMA<sup>31</sup> or neighbor joining<sup>32</sup> cannot display the resulting ambiguity in the data and may prove misleading when defining clusters.<sup>33</sup>

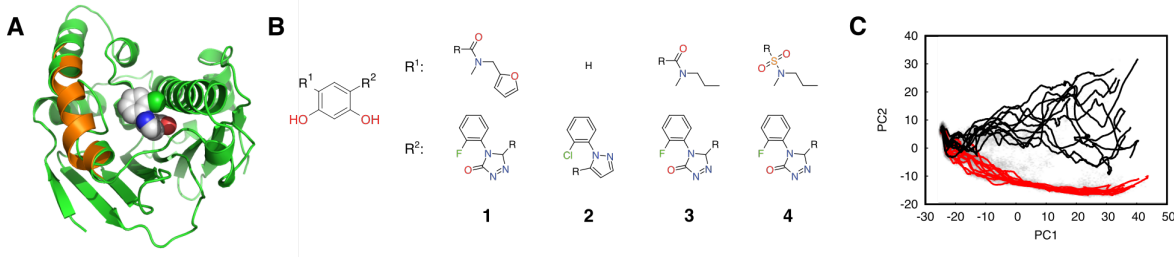


Figure 1: A: Hsp90-ligand complex. Protein in "loop binding" conformation as green cartoon, in "helix binding" conformation in orange. Compound **2** in spheres. B: investigated compound set. C: Training data selected for classifying pathways of **1**, superimposed on a plot of the first two contact PCs. Path 1 in red, path 2 in black. Non-equilibrium biased energy landscape (see Eq. (6)) as gray shading.

In this work, we illustrate two strategies for identifying pathways, assessing the possibility of data bias and uncertainties in the pathway definitions, and assignment of trajectories to the discovered pathways, employing the well-established test system of the N-terminal domain of heat shock protein 90 (Hsp90, Fig. 1a)<sup>34,35</sup> with four sample compounds **1** to **4**

(see Fig. 1b), all of which share a common resorcinol functional group. If initial pathways can be observed in a subset of trajectories within a relevant coordinate space identified via conPCA, we provide a machine learning approach using the gradient boosting technique.<sup>36,37</sup> If initial pathways cannot be attributed, but a suitable distance metric between trajectories is known or can be guessed, we describe the usage of neighbor-nets<sup>38,39</sup> to cluster trajectories in order to identify possible paths. An advantage of using neighbor-nets is that it allows us to take data bias or ambiguities in the input data into account, which improves the quality of the trajectory assignment over clustering via dendrograms such as UPGMA.<sup>40,41</sup> Finally, we describe a case in which pathway separation has to be performed on the basis of a single ligand-internal hydrogen bond.

## Methods

### Dissipation-corrected targeted molecular dynamics (dcTMD)

To set the stage for the topic of this article, we briefly review the basics of dcTMD,<sup>18</sup> the method for which pathway separation is required. Targeted MD makes use of a constant velocity constraint<sup>42</sup>

$$x(t) = x_0 + v_c t \tag{1}$$

where  $x$  is a position along a reaction coordinate of choice (in our case the distance between the centers of mass of two groups of atoms),  $t$  is time and  $v_c$  is the constraint velocity. The constraint is imposed by a constraint force  $f_c$  calculated via a Lagrange multiplier for each time step. Integration of  $f_c$  along  $x$  results in a work  $W(x)$  that is larger than  $\Delta G(x)$ . According to Jarzynski’s equality,<sup>22,23</sup>  $W$  and  $\Delta G$  are related as

$$\Delta G = -k_B T \ln \langle e^{-W/k_B T} \rangle \approx \langle W \rangle - \frac{\langle \delta W^2 \rangle}{2k_B T} = \langle W \rangle - W_{\text{diss}}, \tag{2}$$

where the mean  $\langle \dots \rangle$  is calculated over an ensemble of trajectories initiated from an equilibrium distribution, and  $W_{\text{diss}}$  is the dissipative work. The approximation corresponds to a cumulant expansion truncated after the 2<sup>nd</sup> cumulant. Combining Eq. (2) with a Markovian Langevin equation<sup>20</sup> allows the definition of a friction coefficient

$$\Gamma_{\text{NEQ}}(x(t)) = \frac{1}{k_{\text{B}}T} \int_0^{t(x)} \langle \delta f_{\text{c}}(t) \delta f_{\text{c}}(t - \tau) \rangle d\tau \quad (3)$$

with  $\delta f_{\text{c}} = f_{\text{c}} - \langle f_{\text{c}} \rangle$  and  $W_{\text{diss}} = v_{\text{c}} \int_0^x \Gamma_{\text{NEQ}}(x') dx$ .

The major challenge in the applicability of dcTMD to a set of targeted MD trajectories lies in the validity of the approximation made when truncating the cumulant expansion, which only holds if  $W$  follows a normal distribution<sup>18</sup> within the set of trajectories. The presence of distinct pathways along an additional coordinate orthogonal to the bias coordinate leads to  $W$  becoming multi-modal, leading to a significant overestimation of friction.<sup>19,24</sup> As this coordinate often is not known *a priori* and must be identified for pathway separation, we denote it in the following as a "hidden coordinate". The typical method we use for revealing hidden coordinates is principal component analysis, which is introduced in the following.

## Principal component analysis (PCA)

Principal component analysis (PCA) is a common method to reduce the dimensionality of a system to reveal relevant coordinates underlying a microscopical process of interest.<sup>30,43</sup>

The method builds on the calculation of a covariance matrix

$$\sigma_{mn} = \langle (r_m - \langle r_m \rangle)(r_n - \langle r_n \rangle) \rangle \quad (4)$$

from input coordinates  $\mathbf{r}$ . Diagonalizing this covariance matrix yields  $i$  eigenvalues and -vectors (where  $i$  is the number of unreduced dimensions of the system), describing the direction and variance of the principal motion. Usually, only the first few  $\mathbf{v}^{(i)}$  with the largest eigenvalues that amount to  $\gtrsim 80\%$  of cumulative eigenvalues are chosen for further

analysis. Projecting the original coordinates  $\mathbf{r}$  onto the eigenvectors

$$x_i = \mathbf{r} \cdot \mathbf{v}^{(i)} \quad (5)$$

yields the linearly uncorrelated principal components (PCs)  $x_i$  that can serve as reaction coordinates. In the following, we use residue contact distances as  $\mathbf{r}$ . It should be noted that the definition of time-independent means  $\langle r_i \rangle$  in Eq. (4) in principle only applies to equilibrium MD data. Recently, PCA was extended to nonequilibrium TMD data,<sup>44</sup> and we used the  $\langle r_i \rangle$  calculated over both time and ensemble of the nonequilibrium trajectories as reference.

For contact analysis, we used all residues for which a minimum distance of 4.5 Å to the ligand (by center of mass) in any time frame in any pulling trajectory is reached. This results in 27 reference residues that are displayed in Fig. S1. These residue-ligand center-of-mass distances  $\mathbf{r}(t)$  were subjected to PCA. Projections on the first three eigenvectors were plotted as histograms to reveal possible pathways in the form of "valleys" in their biased energy landscape<sup>44,45</sup>

$$\Delta\mathcal{G}_i = -k_B T \ln(P(x_i)). \quad (6)$$

$\Delta\mathcal{G}$  is defined such that the underlying probability distributions can be qualitatively compared with free energy profiles from equilibrium calculations. An illustration of  $\Delta\mathcal{G}$  and trajectories passing through two distinct pathways is provided by Figs. 1c and S2a.

## Machine learning for pathway classification

Following conPCA and visual identification of pathways in the PC space, we employed the XGBoost algorithm,<sup>36</sup> using the implementation developed by Brandt et al.,<sup>37</sup> to learn features of trajectories following individual pathways. The algorithm is supplied with pre-classified training data from the ensemble, manually labeled according to pathway. The selection of trajectories for training data was based on two factors: 1) trajectories should be

unambiguously assignable by visual inspection to a single pathway, i.e. no crossover between pathways during the course of the trajectory; and 2) given the above, trajectories should nonetheless vary as much as possible. This ensures the model is trained with 'clean' yet representative data.

A test/train split of 70/30 was employed. 100 training rounds were completed with learning rate set to 0.3 and maximum tree depth to 6 to construct a prediction model capable of assigning a pathway to unseen data. Training data was supplied as individual trajectory frames  $\mathbf{r}(t)$  together with the visual pathway assignment. Data consisted of the 27 raw contacts used as predictor variables, and the manually assigned pathway as the target variable. As differences between the pathways were not clearly visible at the start of the trajectories, data in this initial region of the trajectories (in the case of Fig. 1 c, all points with PC1 < -15) were assigned to a 'neutral class' which did not contribute to prediction, in order to avoid confusing the algorithm.

The model constructed was then used to predict the pathway taken by the remaining trajectories for all  $\mathbf{r}(t)$ . Once predictions were completed for individual time points, a score  $S$  for each trajectory and path  $j$  was calculated based on all  $N$  time steps  $i$  in a trajectory as

$$S_j = \frac{1}{N} \sum_i^N \delta_j \quad \text{with } \delta_j = \begin{cases} 1, & \text{if } \mathbf{r}_i(t) \in j \\ 0, & \text{otherwise.} \end{cases} \quad (7)$$

Points classified to the neutral state were ignored. All trajectories with  $S_j > 0.8$  were classified as belonging to path  $j$ . Trajectories which did not meet this cut-off for any pathway remained unclassified.

## RMSD trajectory clustering

As conPCA is based on contact distances between the ligand and residue center-of-masses, it is blind to changes in ligand conformation or rotation, which might also constitute hidden coordinates. Thus, efforts were made to develop a method capable of resolving such small-

scale changes. To do so, we first aligned all trajectories based on a fit of the  $C_\alpha$  atoms of the protein to provide a coordinate reference for ligand unbinding. After fitting, we calculated the time-dependent root mean square distance (RMSD)

$$d_{ij}(t) = \sqrt{\frac{1}{N} \sum_{k=1}^N \|\mathbf{l}_{jk}(t) - \mathbf{l}_{ik}(t)\|^2} \quad (8)$$

between any pair of trajectories  $i$  and  $j$  for all  $N$  ligand atoms  $k$  with Cartesian position vectors  $\mathbf{l}$ . Averaging all  $d_{ij}(t)$  over time yields a RMSD matrix that encodes the dissimilarity of trajectories according to the relative position of ligand atoms.

Having obtained the matrix, we used the distances to classify trajectories into clusters according to their similarity and interpreted these clusters as pathways. The problem is analogous to that of constructing a phylogenetic tree from genetic data depicting the evolutionary relationships between various species.<sup>33</sup> Two methods for clustering from distance data are therefore borrowed from the field of phylogenetics, which we introduce in the following.

### Unweighted pair group method using arithmetic averages (UPGMA)

The unweighted pair group method using arithmetic averages (UPGMA)<sup>40,41</sup> is a bottom-up approach for construction of dendrograms, also known as phylogenetic trees, from a distance matrix.<sup>40,41</sup> At first, each "leaf" of the tree (here, each trajectory) is considered to exist in its own cluster  $C$  (called "node" in the following). The two nodes  $i$  and  $j$  which have the smallest  $d_{ij}$  are merged into a single united node  $k$ . The distances between the new node  $k$  and the remaining nodes are calculated as

$$d_{kl} = \frac{d_{il}|C_i| + d_{jl}|C_j|}{|C_i| + |C_j|} \quad \text{and} \quad |C_k| = |C_i| + |C_j|, \quad (9)$$

where  $|C_i|$  is the number of initial nodes, i.e., trajectories, in  $i$ , while  $l$  is one of the other nodes that are not merged. The distance matrix is then updated with these new distances. Subsequently, node-merging is repeated iteratively on the respective two closest remaining

nodes until all nodes are merged.

## Neighbor-net

One major problem associated with dendrograms, whether calculated using UPGMA or a similar method such as neighbor-joining,<sup>32</sup> is that they do not take into account uncertainties in the input data. Especially if the elements in the distance matrix are similar to each other, inaccuracies caused, e.g., by problems with the initial superposition of the protein coordinates, might become dominant over the information in the individual distance pairs.<sup>33</sup> In other words, dendrograms do not provide the equivalent of an error bar.

To allow such a representation, we here turn to the neighbor-net algorithm.<sup>39,46</sup> In this algorithm, the amalgamation procedure does not immediately unite a pair of nodes, but waits until the pair is united with a third node, upon which the amalgamation step replaces three nodes with two (see Ref.<sup>33</sup> for a detailed description). In this way, a network is calculated, which forms a superposition of several possible dendrograms contained within the data. If the input data exhibits a clear tree-like hierarchy, the neighbor-net collapses into a unique dendrogram. On the other hand, if ambiguity is present in the data, a network of equidistant nodes resembling a "spider net" appears, which represents the desired equivalent of an error bar. A decision can then be made where to impose cluster boundaries on the neighbor-net.

## Simulations of Hsp90-ligand complexes

Simulations were performed using the open-source Gromacs software<sup>47</sup> v2018 using the AMBER99SB forcefield<sup>48,49</sup> and the TIP3P water model.<sup>50</sup> We performed simulations on four Hsp90-binding compounds named **1**, **2**, **3** and **4**, which are compounds **1b** (PDB ID 5J20),<sup>51</sup> **1j** (PDB ID 6FCJ),<sup>52,53</sup> **1f** (modeled based on PDB ID 5J9X)<sup>51</sup> and **1g** (PDB ID 5J27)<sup>10</sup> in Ref.,<sup>53</sup> respectively. The simulation systems and topologies were taken from Ref.<sup>53</sup> Here, ligand topologies were created with antechamber<sup>54</sup> and acpype<sup>55</sup> using GAFF parameters<sup>56</sup> and AM1-BCC charges.<sup>57,58</sup> Simulations were performed using PME for electrostatics<sup>59</sup> with

a minimal real space cut-off of 1 nm and a van der Waals cut-off of 1 nm. Hydrogen atom bonds were constrained via the LINCS algorithm.<sup>60</sup> For each ligand, statistically independent equilibration runs were performed (1000 for **1**, 500 for **2**, 100 for **3** and 513 for **4**, respectively) in the NPT ensemble at 300 K and 1 bar, using the Berendsen thermostat and barostat,<sup>61</sup> with an integrator time step of 2 fs and a trajectory length of 100 ps. Non-equilibrium TMD calculations using the Gromacs PULL code in constraint mode were then performed by continuing the equilibration runs for 2 ns in the NPT ensemble at 300 K and 1 bar, using the Nosè-Hoover thermostat<sup>62</sup> and Parrinello-Rahman barostat<sup>63</sup> with a fixed constraint velocity of 1 m/s and an integration step size of 1 fs. Values for the constraint forces were saved at each time step, while structural snapshots were written out each picosecond. The first pulling group was defined using all C $_{\alpha}$  atoms of the  $\beta$ -sheet forming the ligand binding site, while the second group was defined using the ligand heavy atoms (see Ref.,<sup>53</sup> Fig. S1).

## General data analysis

Analysis was performed using the programming language Python, making particular use of the packages NumPy,<sup>64</sup> SciPy<sup>65</sup> and Pandas<sup>66</sup> for data analysis, as well as MDAnalysis<sup>67</sup> for extracting data from MD files. The XGBoost method was used in form of the xgbAnalysis package.<sup>37</sup> UPGMA trees were calculated using SciPy,<sup>65</sup> while neighbor-nets are calculated and displayed via the implementation in SplitsTree.<sup>68</sup> Matplotlib<sup>69</sup> and Gnuplot<sup>70</sup> were used for generating 2D plots, and Mayavi<sup>71</sup> for 3D plots. VMD<sup>72</sup> and Pymol<sup>73</sup> were used for graphical visualization of structures and MD trajectories.

# Results and Discussion

## Pathway attribution for compound 1 by principal component analysis (PCA) and machine learning

Initially, we developed and tested methods for pathway separation using compound 1. Figure S3 shows cumulative eigenvalues for the principal components from conPCA, which reach 0.8 for the second and 0.95 for the third PC. As a result, two PCs (Fig. S4) are sufficient to describe the system, with additional detail provided by the third, which is easily rationalized as an internal coordinate representation of the three Cartesian coordinates the ligand can diffuse along. Figures S2b and S2c show the location of the four residues that contribute most strongly to the value of the first two principal components. For PC1, these are located beneath the binding site: because it represents the largest variance in the data, PC1 correlates very strongly with the pulling coordinate. The residues that contribute most strongly to PC2 are concentrated at one edge of the binding site, so PC2 varies based on how close the ligand passes to this region. Inspection of the coordinates by means of 2D and 3D plots revealed two main pathways for ligand dissociation (Fig. S2a and Supplementary Movie 1). The first two principal components suffice to distinguish the two pathways, though a three-dimensional plot including the third PC facilitates their identification. Pathway 1 passes close to the residues highlighted in Fig. S2c (low PC2, black line in Fig. 1c) and the pathway 2 far from it (high PC2, red line in Fig. 1c). Therefore, the two pathways, concretely considered, are two routes out of the protein on opposite sides of the binding site as displayed in Fig. 2a,b.

We then used our machine learning procedure to score trajectories according to the pathway taken. Twenty trajectories (ten for each path; examples shown in Fig. 1c) were selected by visual inspection for model training, and the resulting model used to assign each point of every trajectory studied to one of the two pathways. A histogram of scores for path 1 is depicted in Fig. 2c. As most of the values can be seen to cluster near 0 and 1,

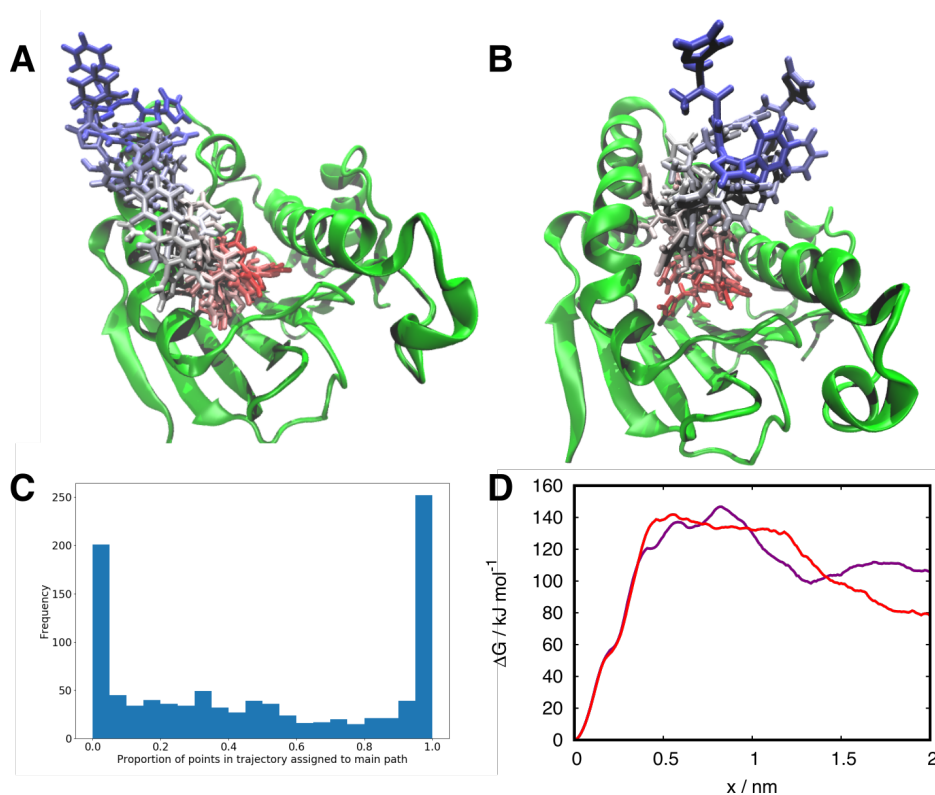


Figure 2: A,B: Example trajectories for the two pathways 1 (A) and 2 (B). Ligand **1** positions are shown at 0.2 ns intervals and colored accordingly (red at the start of the trajectory, blue at the end.) C: Histogram of compound **1** ML scores for ensemble of 1000 trajectories for path 1. Values  $> 0.8$  correspond to path 1, values  $< 0.2$  to path 2. D: Free energy plots for **1** pathways (from total ensemble of 1000 trajectories) as separated by PCA-ML (purple: path 1, 333 trajectories; red: path 2, 320 trajectories)

a sufficiently large class of trajectories could be obtained for both pathways, by selecting trajectories with  $S_j > 0.8$  for path 1 and  $S_j < 0.2$  for path 2 as described in the Methods, and a free energy profile was calculated using the dcTMD method.

Values for 'importance' of each contact, i.e. the extent of its contribution to the model, can also be extracted,<sup>37</sup> permitting a comparison with the results from PCA. Three contacts (Phe134, Val136 and Val186, see Fig. S5) in particular have high values summing to 0.86 (implying 86% of the model's predictive power is derived from these three contacts, see Tab. S1). Comparing with Fig. S4, residue 186 is one of the largest contributors to PC1, while contacts 134 and 136 are two of the largest contributors to PC2, showing the model has a similar opinion on the interpretation of the contact data as conPCA.

The free energy curves for the PCA-ML pathways are given in Fig. 2d. It can be observed that both pathways exhibit no friction overestimation artefact,<sup>24</sup> but free energy differences between bound and unbound states of  $\sim 80\text{--}100$  kJ/mol appears unrealistically large given an experimental<sup>51</sup>  $K_D$  of  $\sim 5 \cdot 10^{-9} \text{M}^{-1}$  (which, ignoring corrections,<sup>74</sup> would correspond to a standard free binding energy  $\Delta G_0 \sim 50$  kJ/mol). We therefore check in the following if RMSD-based clustering results in more reasonable free energy profiles.

## Trajectory clustering from RMSD data

As an alternative to performing analysis based on pathways pre-defined by a human operator, we wanted to formulate a method that gives an unbiased estimate of similarities between trajectories, allowing for a bottom-up pathway identification similar to a density-based clustering<sup>75</sup> of MD data that is closer to the full dimensionality of the input data. The result was our RMSD-based clustering, which is presented in the following. RMSD values were extracted from 500 trajectories of compound **1**, which yielded a distance matrix, a representation of which is given for illustrative purposes in Fig. S6. Hierarchical clustering using the UPGMA algorithm returned the dendrogram given in Fig. 3a. Based on the dendrogram, a cut-off distance of 4.8 was selected to yield several clusters, three of which are sufficiently populated ( $> 50$  trajectories)<sup>19</sup> to carry out a free energy analysis (Fig. 3c). In comparison to the PCA-ML approach, we observe the emergence of one additional pathway. Path 1 exhibits a final unbinding free energy of  $\sim 60$  kJ/mol, which is more reasonable than the results from PCA-ML-based sorting. Path 2 exhibits a  $\Delta G$  profile roughly similar to those found using PCA-ML, while the novel path 3 exhibits an unreasonable drop to negative values as in a friction overestimation artefact, which suggests at least some of the trajectories are still assigned wrongly.

To improve trajectory attribution, clustering using the neighbor-net algorithm was performed on the same data set as UPGMA clustering (500 trajectories), which yields the network in Fig. 3b. Three regions were identified where trajectories are more densely and

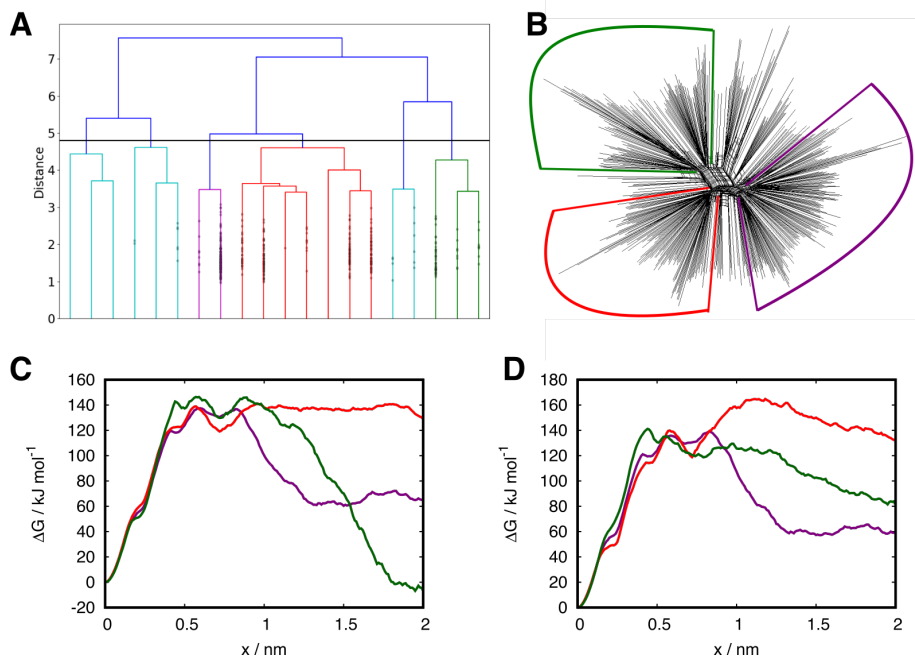


Figure 3: A: Dendrogram of clustered **1** trajectories (only first 20 splits shown; additional splits are indicated by small grey circles). Imposing a cut-off at 4.8 (horizontal black line) gives six clusters, with populations of 177 (purple), 227 (red) and 62 (green); the remaining three, colored in cyan, have populations of 5, 14 and 14, and are not used for free energy calculations. B: Network diagram produced by neighbor-net algorithm. The radiating lines represent nodes (i.e. trajectories), and the line lengths represent RMSD distances. Ambiguous node merging is visible in the center. Three main clusters are visible, while some trajectories (especially on the upper right) do not unambiguously fit into any larger cluster. Colored lines represent cluster boundaries chosen by a human operator. C: Free energy profiles for pathways from RMSD (UPGMA) clustering: path 1 (purple, population 177), path 2 (red, population 227), and path 3 (green, population 62)]. D: Free energy profiles for pathways from RMSD (neighbor-net) clustering: path 1 (purple, population 166), path 2 (red, population 106), and path 3 (green, population 124).

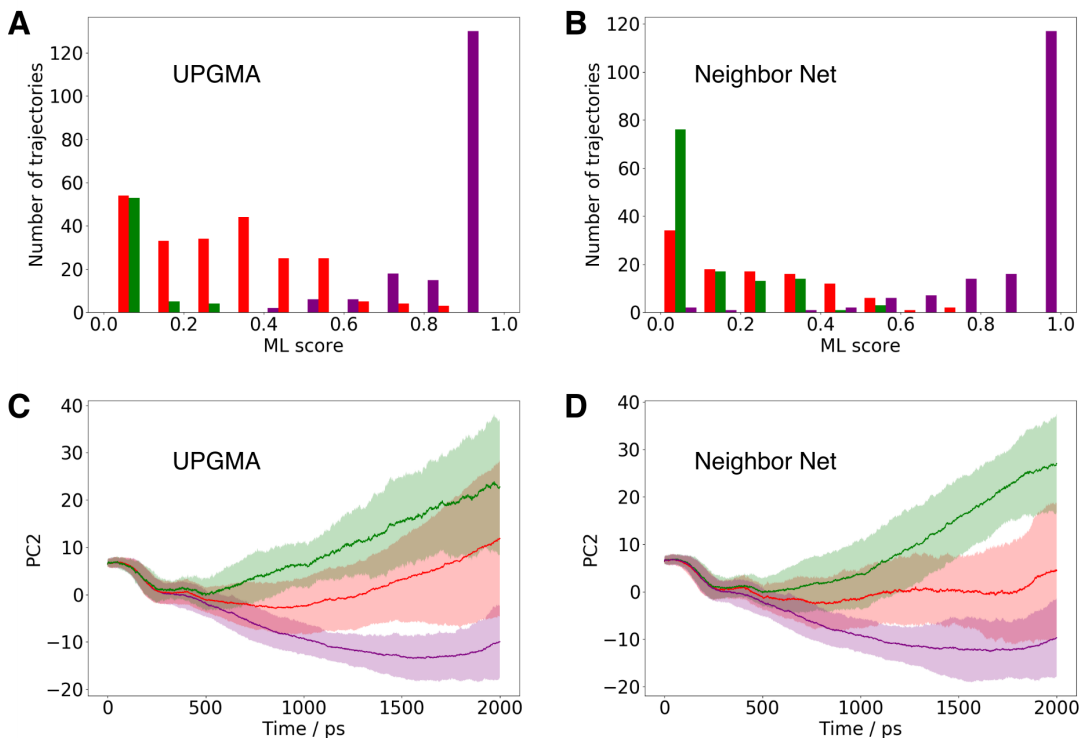


Figure 4: A, B: ML scores for paths clustered by both UPGMA and neighbor-net as presented in Fig. 3 using the same coloring scheme. C,D: Average PC2 value for RMSD clusters of trajectories plotted against time with standard deviation shading.

unambiguously located, and on this basis three clusters are defined, excluding the remainder of the trajectories. Free energy analysis was performed on both classes, yielding results in Fig. 3d. It can be seen that the path 1 (purple) dcTMD curve provides very similar information to path 1 produced by the UPGMA clustering. The two classes identified in each case for path 1 have almost identical composition (147 trajectories in common out of populations of 177 in UPGMA and 166 in neighbor-net). While path 2 (red) now exhibits an additional barrier at  $x \sim 1.2$  and ends with an unreasonably high final  $\Delta G \sim 140$  kJ/mol, the new path 3 (green) ends at a free energy similar to path 1 and thus seems to be better resolved.

To check the source of the improved  $\Delta G$  along path 3, we compare the pathways derived from RMSD clustering with the PCA-ML analysis. Figure 4a,b shows the ML scores of the trajectories for each of the classes, demonstrating that path 1 (purple class) in both approaches corresponds to the PCA-ML path 1. Concerning paths 2 (red class) and 3 (green

class), it turns out that path 3 actually corresponds to path 2 from PCA-ML, while path 2 represents a movement between both paths. Figs. 4c,d indeed show that the "green" trajectories are those which follow the opposite side of the binding site to the PCA-ML path 1, while the "red" trajectories follow a more neutral course through the middle between both paths. This attribution explains the significantly higher  $\Delta G$  of path 2, as the ligand is pushed through several protein residues, applying work to the protein fold. The neighbor-net algorithm indeed improves the attribution of trajectories towards path 2 and reduces the population of path-intermediate trajectories.

Overall, RMSD clustering can be considered an improvement over the PCA-ML based data, with neighbor-net based clustering being superior to UPGMA clustering. A limitation of RMSD clusters however is the lack in information regarding the physical meaning of the pathways they represent. conPCA here is able to complement RMSD clustering, as it reveals more information on the Cartesian origins of such pathways.

## Pathway separation of further ligands

Following testing of the pathway separation methods above with **1**, the applicability to the three other Hsp90 ligands **2**, **3** and **4** was tested. First of all, conPCA is performed, using the same contacts as for **1**, but diagonalizing the covariance matrix anew for each ligand, which provides different eigenvectors for each PCA. We focus first on compound **2**, which differs from **1** in that it binds to Hsp90 in the loop conformation, rather than the helix conformation. Here, the PCs again reveal two pathways. Unlike **1**, for which path 1 dominates, path 2 is far more heavily populated for **2**.

The PCA-ML pathway separation again yields two pathways, while RMSD/neighbor-net clustering splits one of the two paths into two sub-paths (see Fig. 5a,b), as well. As for **1**, the pathways pass along opposite sides of the binding site surface (Fig. 5b). One of the two sub-paths (in red) gives unrealistic results, this time in the form of unreasonably low final

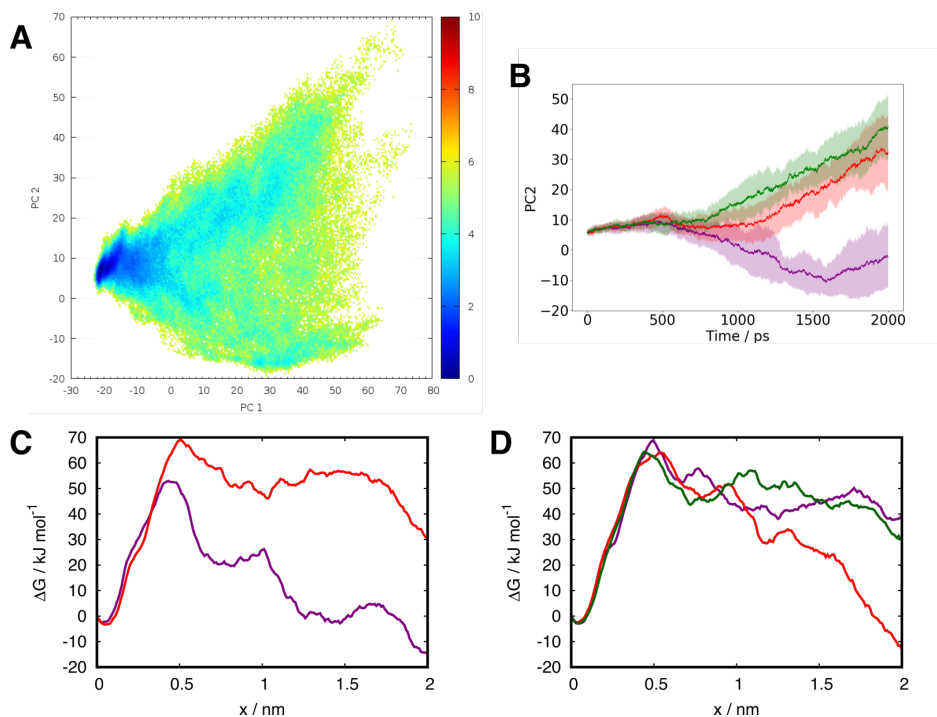


Figure 5: A: Biased energy diagram<sup>44</sup>  $\Delta\mathcal{G}$  for first two PCs of compound **2**. B: average PC2 value for RMSD/neighbor-net clusters plotted against time, with standard deviation as shading. Purple represents path 1, green and red represent two alternative definitions for path 2. C,D: free energy plots for (C) PCA-ML and (D) RMSD clusters.

$\Delta G$  values due to mixing of trajectories from different paths. The results of **2** again suggest RMSD clustering provides better pathway separation than PCA-ML. Indeed, we used path 1 (purple in Fig. 5d) identified via RMSD clustering in our Langevin equation simulations and analysis on binding and unbinding rate constants as well as  $K_D$  and found good agreement with experimental values.<sup>19</sup>

To highlight problems one may encounter in the pre-choice of a suitable input coordinate set, we now turn to an interesting case where we found that a small chemical difference between two ligands results in the appearance of an unexpected ligand-internal hidden coordinate. Compounds **3** and **4** share a very similar structure (Fig. 1b), differing only in the replacement of the amide moiety in **3** with a sulfonamide in **4**. As can be seen in Fig. 6, both ligands appear to exhibit similar biased energy  $\Delta\mathcal{G}$  profiles. A dissipation correction as given in Fig. 6c however shows that despite the small chemical difference, **3** does not exhibit the

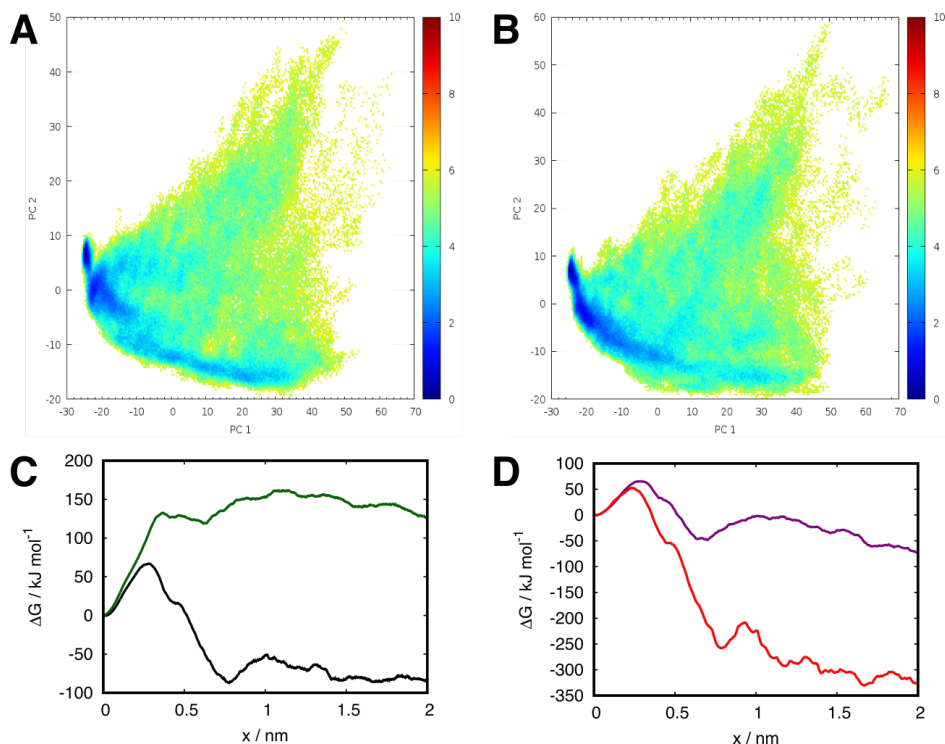


Figure 6: A,B: Biased energy profiles  $\Delta\mathcal{G}$  along first two PCs for **3** (A) and **4** (B). C: free energies of **3** (green) and **4** (black) without pathway separation. D: **4** pathways in PCA-ML.

friction overestimation artefact even without applying pathway separation, while **4** clearly does. Furthermore, PCA-ML on **4** fails to remove the artefact, which still is present for both possible pathways displayed in Fig. 6, with RMSD clustering failing as well.

Searching for a suitable hidden coordinate to perform pathway separation, visual inspection of trajectories (Fig. 7a) revealed a key difference between the two chemically similar ligands: **4** can form an internal hydrogen bond between the sulfonyl and one of the hydroxyl groups on the adjacent resorcinol ring. When the hydrogen bond is present, rigidity is enforced on the ligand, while a contact with surrounding water can break the hydrogen bond and result in increased conformational dynamics during dissociation. Such a hydrogen bond does not exist with the amide group in **3** due to the lower electrostatic charge on the carbonyl vs. the sulfonyl oxygen atoms ( $-0.58 e$  vs.  $-0.66 e$ ). Thus, we carried out a separation of trajectories into two classes according to formation (or lack thereof) of this internal hydrogen bond as shown in Fig. 7b and Tab. S2 during the first 0.25 ns of simulation, i.e., before the

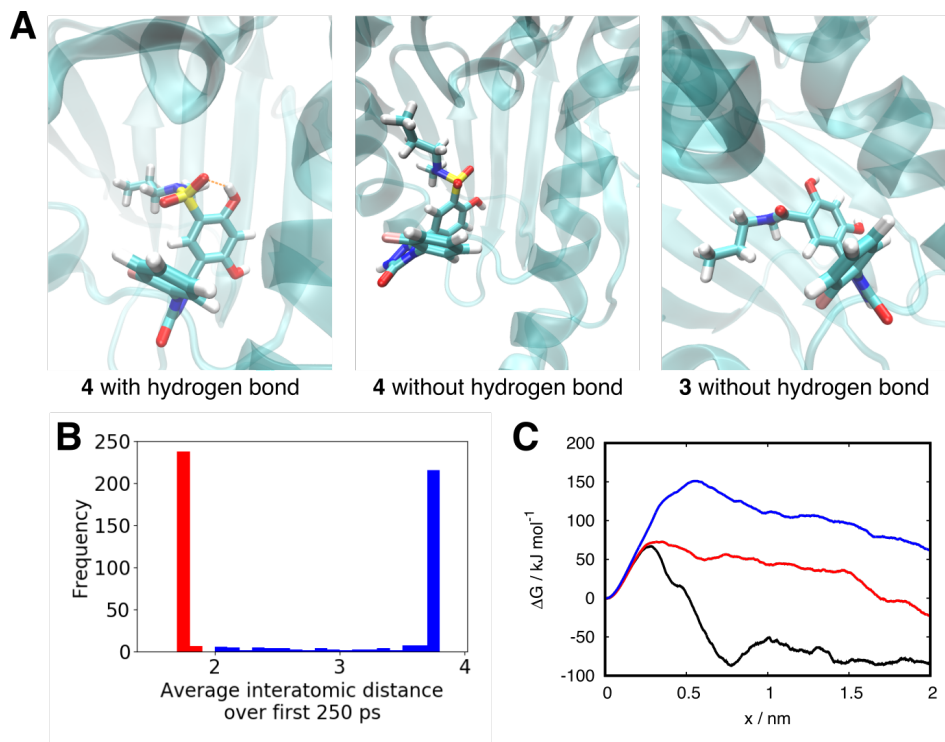


Figure 7: A: Structures of ligands **3** and **4** during unbinding. B: separation of trajectories with (red) and without (blue) ligand-internal hydrogen bond. C: free energy profiles for compound **4**, unseparated (black), with (red) and without (blue) hydrogen bond.

transition barrier in Fig. 7c. If the average hydrogen-oxygen distance during this time period between the investigated groups was lower than 2 Å, the hydrogen bond was considered to be present. As can be seen in the  $\Delta G$  curves in Fig. 7c, the friction overestimation artefact is no longer evident in both of the two resulting pathways in hydrogen bond distance. For the pathway without hydrogen bond, the profile appears very similar to that for **3**, as would be expected. We note that the  $\Delta G$  profile of the pathway with hydrogen bond still exhibits a drop in the free energy in the final 0.5 ns, probably from an additional hidden coordinate that we do not resolve here.

## Conclusion

The aim of this project was to develop and test methods for separating dcTMD trajectories into pathways, in order to remove the influence of hidden coordinates, which result in

a overestimation of the dissipation correction. conPCA allowed identification of pathways for Hsp90. On this basis, a machine learning model could be built, which automated the classification of trajectories to one of the pathways that were identified by visual inspection. Applying this method, dubbed PCA-ML, facilitates pathway classification for dcTMD compared to purely visual inspection. The other main method applied to characterize the ligand dissociation route was RMSD-based clustering. The method is capable of resolving sub-pathways contained within those produced by PCA-ML. From this result was reasoned that, in general, while PCA-ML is effective at identifying pathways through a protein in general, RMSD clustering gives superior performance when determining the composition of the trajectory classes. In particular, the ability of neighbor-nets to resolve ambiguity in the input data improves the attribution of trajectories to pathways. For carrying out a pathway correction, the following workflow is proposed: first of all, as many trajectories as possible should be collected ( $\gtrsim 500$ ), and conPCA performed. If it is possible, on this basis, to identify clearly separated pathways, a machine-learning model should be built to classify trajectories. In parallel, RMSD clustering should be performed, and the composition of the classes produced by both classifications compared. If it is not possible to perform PCA-ML, the RMSD pathways should at least be plotted in the PCA space, or the trajectories inspected using graphics software, to ensure that they have a reasonable physical meaning. If PCA-ML and RMSD return pathway classes with similar composition, this is a good sign that the pathway attribution is sound. However, the composition as determined by RMSD should be considered more trustworthy than that produced by PCA-ML, because it takes ligand conformation changes into account.

Closing this work, we are aware that both PCA-ML and RMSD-based clustering as presented here are tools that can assist a researcher with classifying trajectories into pathways, but require a large amount of human input in the pre-choice of trajectories in training the machine model, of setting cut-off levels in UPGMA trees, or of boundaries between paths in neighbor-nets. The resulting paths are therefore still potentially affected by human bias. In

coming works, we will therefore evaluate clustering algorithms that all but eliminate human input, and reduce the number of free parameters to a minimum. Lastly, a researcher performing a pathway analysis has to be aware that already small chemical differences between ligands can lead to clearly different unbinding pathways, and that the search for the underlying hidden coordinate can be tedious and requires visual inspection as well as considerable chemical intuition. While this insight appears to be frustrating, it relates to the general problem and difficulties of how to identify reaction coordinates for biomolecular processes,<sup>76</sup> which is one of the major current topics in biomolecular simulations method development.

## Data and software availability

dcTMD analysis scripts as well as the fastpca and xgbAnalysis program packages are available at <https://www.moldyn.uni-freiburg.de/software.html>. Simulation data, especially Hsp90 simulation start structures and system topologies are available from the authors upon request.

## Acknowledgement

This work has been supported by the Deutsche Forschungsgemeinschaft (DFG) via grant WO 2410/2-1 within the framework of the Research Unit FOR 5099 "Reducing complexity of nonequilibrium" (project No. 431945604), the High Performance and Cloud Computing Group at the Zentrum für Datenverarbeitung of the University of Tübingen, the state of Baden-Württemberg through bwHPC and the DFG through grant no INST 37/935-1 FUGG (RV bw16I016) and the Freiburg Institute for Advanced Studies (FRIAS) of the Albert-Ludwigs-University Freiburg. The authors are grateful to Gerhard Stock, Matthias Post, Victor Tänzler and Moritz Schäffler (all University of Freiburg) for helpful discussions.

## Supplementary Information

Four Supplementary Figures detailing on the results from conPCA of **1** (Figs. S1 to S4), one Supplementary Figure (Fig. S5) and one Supplementary Table (Tab. S6) with information on most important residues in the machine learning procedure, one Supplementary Figure (Fig. S6) with an example RMSD matrix, and one Supplementary Table (Tab. S2) with statistics on path separation of compounds **3** and **4**. (PDF).

## References

- (1) Wodak, S. J. et al. *Structure* **2019**, *27*, 566–578.
- (2) Schuetz, D. A. et al. *Drug Discov. Today* **2017**, *22*, 896–911.
- (3) Bruce, N. J.; Ganotra, G. K.; Kokh, D. B.; Sadiq, S. K.; Wade, R. C. *Curr. Opin. Struct. Biol.* **2018**, *49*, 1–10.
- (4) De Benedetti, P. G.; Fanelli, F. *Drug Discov. Today* **2018**, *23*, 1396–1406.
- (5) Swinney, D. C. *Pharm. Med.* **2012**, *22*, 23–34.
- (6) Copeland, R. A. *Nat. Rev. Drug Discov.* **2015**, *15*, 87–95.
- (7) Tiwary, P.; Limongelli, V.; Salvalaglio, M.; Parrinello, M. *Proc. Natl. Acad. Sci. U.S.A.* **2015**, *112*, E386–E391.
- (8) Shekhar, M.; Smith, Z.; Seeliger, M.; Tiwary, P. *Angew. Chem. Int. Ed.* **2022**,
- (9) Lüdemann, S. K.; Lounnas, V.; Wade, R. C. *J. Mol. Biol.* **2000**, *303*, 797–811.
- (10) Kokh, D. B.; Amaral, M.; Bomke, J.; Grädler, U.; Musil, D.; Buchstaller, H.-P.; Dreyer, M. K.; Frech, M.; Lowinski, M.; Vallee, F.; Bianciotto, M.; Rak, A.; Wade, R. C. *J. Chem. Theory Comput.* **2018**, *14*, 3859–3869.

- (11) Tsujishita, H.; Moriguchi, I.; Hirono, S. *J. Phys. Chem.* **1993**, *97*, 4416–4420.
- (12) Schuetz, D. A.; Richter, L.; Amaral, M.; Grandits, M.; Grädler, U.; Musil, D.; Buchstaller, H.-P.; Eggenweiler, H.-M.; Frech, M.; Ecker, G. F. *J. Med. Chem.* **2018**, *61*, 4397–4411.
- (13) Bianciotto, M.; Gkeka, P.; Kokh, D. B.; Wade, R. C.; Minoux, H. *J. Chem. Theory Comput.* **2021**, *17*, 6522–6535.
- (14) Huber, G.; Kim, S. *Biophys. J.* **1996**, *70*, 97–110.
- (15) Votapka, L. W.; Jagger, B. R.; Heyneman, A. L.; Amaro, R. E. *J. Phys. Chem. B* **2017**, *121*, 3597–3606.
- (16) Berendsen, H. J. *Simulating the Physical World: Hierarchical Modeling from Quantum Mechanics to Fluid Dynamics*; Cambridge University Press, 2007.
- (17) Leach, A. R. *Molecular Modeling*; Pearson Education Limited: London, 1996.
- (18) Wolf, S.; Stock, G. *J. Chem. Theory Comput.* **2018**, *14*, 6175–6182.
- (19) Wolf, S.; Lickert, B.; Bray, S.; Stock, G. *Nat. Commun.* **2020**, *11*, 2918.
- (20) Zwanzig, R. *Nonequilibrium Statistical Mechanics*; Oxford University: Oxford, 2001.
- (21) Bussi, G.; Parrinello, M. *Phys. Rev. E* **2007**, *75*, 2289–7.
- (22) Jarzynski, C. *Phys. Rev. Lett.* **1997**, *78*, 2690–2693.
- (23) Hendrix, D. A.; Jarzynski, C. *J. Chem. Phys.* **2001**, *114*, 5974–5981.
- (24) Jäger, M.; Koslowski, T.; Wolf, S. *J. Chem. Theory Comput.* **2022**, *18*, 494–502.
- (25) Bolhuis, P. G.; Chandler, D.; Dellago, C.; Geissler, P. L. *Annu. Rev. Phys. Chem.* **2002**, *53*, 291–318.

- (26) Hénin, J.; Lelievre, T.; Shirts, M. R.; Valsson, O.; Delemotte, L. *arXiv.org* **2022**,
- (27) Nguyen, H. L.; Thai, N. Q.; Li, M. S. *J. Chem. Theory Comput.* **2022**,
- (28) Lung, J.; Chen, K.-L.; Hung, C.-H.; Chen, C.-C.; Hung, M.-S.; Lin, Y.-C.; Wu, C.-Y.; Lee, K.-D.; Shih, N.-Y.; Tsai, Y. H. *Drug Des. Devel. Therapy* **2017**, *11*, 3281.
- (29) Nunes-Alves, A.; Kokh, D. B.; Wade, R. C. *Curr. Res. Struct. Biol.* **2021**, *3*, 106–111.
- (30) Ernst, M.; Sittel, F.; Stock, G. *J. Chem. Phys.* **2015**, *143*, 244114.
- (31) Sokal, R. R. *Univ. Kansas, Sci. Bull.* **1958**, *38*, 1409–1438.
- (32) Saitou, N.; Nei, M. *Mol. Biol. Evol.* **1987**, *4*, 406–425.
- (33) Huson, D. H.; Rupp, R.; Scornavacca, C. *Phylogenetic Networks: Concepts, Algorithms and Applications.*; Cambridge University Press: Cambridge, United Kingdom, 2010.
- (34) Schopf, F. H.; Biebl, M. M.; Buchner, J. *Nat. Rev. Mol. Cell Biol.* **2017**, *18*, 345.
- (35) Pearl, L. H.; Prodromou, C. *Annu. Rev. Biochem.* **2006**, *75*, 271–294.
- (36) Chen, T.; Guestrin, C. XGBoost: A Scalable Tree Boosting System. Proceedings of the 22nd ACM SIGKDD International Conference on Knowledge Discovery and Data Mining. New York, NY, USA, 2016; pp 785–794.
- (37) Brandt, S.; Sittel, F.; Ernst, M.; Stock, G. *J. Phys. Chem. Lett.* **2018**, *9*, 2144 – 2150.
- (38) Bryant, D. *Mol. Biol. Evol.* **2003**, *21*, 255–265.
- (39) Levy, D.; Pachter, L. *Adv. Appl. Mathemat.* **2011**, *47*, 240–258.
- (40) Sneath, P. H. A.; Sokal, R. R. *Numerical taxonomy. The principles and practice of numerical classification.*; W.H. Freeman: San Francisco, USA, 1973.
- (41) Wheeler, T. J.; Kececioğlu, J. D. *Bioinformatics* **2007**, *23*, i559–i568.

- (42) Schlitter, J.; Engels, M.; Krüger, P. *J. Mol. Graph.* **1994**, *12*, 84–89.
- (43) Sittel, F.; Stock, G. *J. Chem. Phys.* **2018**, *149*, 150901–150915.
- (44) Post, M.; Wolf, S.; Stock, G. *J. Chem. Phys.* **2019**, *150*, 204110.
- (45) Lickert, B.; Wolf, S.; Stock, G. *J. Phys. Chem. B* **2021**, *125*, 8125–8136.
- (46) Bryant, D.; Moulton, V. *Mol. Biol. Evol.* **2004**, *21*, 255–265.
- (47) Abraham, M. J.; Murtola, T.; Schulz, R.; Páll, S.; Smith, J. C.; Hess, B.; Lindahl, E. *SoftwareX* **2015**, *1–2*, 19 – 25.
- (48) Hornak, V.; Abel, R.; Okur, A.; Strockbine, B.; Roitberg, A.; Simmerling, C. *Proteins* **2006**, *65*, 712–725.
- (49) Best, R. B.; Hummer, G. *Phys. Rev. Lett.* **2006**, *96*, 228104.
- (50) Jorgensen, W. L.; Chandrasekhar, J.; Madura, J. D.; Impey, R. W.; Klein, M. *J. Chem. Phys.* **1983**, *79*, 926.
- (51) Amaral, M.; Kokh, D. B.; Bomke, J.; Wegener, A.; Buchstaller, H. P.; Eggenweiler, H. M.; Matias, P.; Sirrenberg, C.; Wade, R. C.; Frech, M. *Nat. Commun.* **2017**, *8*, 2276.
- (52) Güldenhaupt, J.; Amaral, M.; Kötting, C.; Schartner, J.; Musil, D.; Frech, M.; Gerwert, K. *Angew. Chem. Int. Ed.* **2018**, *57*, 9955–9960.
- (53) Wolf, S.; Amaral, M.; Lowinski, M.; Vallée, F.; Musil, D.; Güldenhaupt, J.; Dreyer, M. K.; Bomke, J.; Frech, M.; Schlitter, J.; Gerwert, K. *J. Chem. Inf. Model.* **2019**, *59*, 5135–5147.
- (54) Wang, J.; Brüschweiler, R. *J. Chem. Theory Comput.* **2006**, *2*, 18–24.
- (55) Sousa da Silva, A. W.; Vranken, W. F. *BMC Res. Notes* **2012**, *5*, 1–8.

- (56) Wang, J.; Wolf, R. M.; Caldwell, J. W.; Kollman, P. A.; Case, D. A. *J. Comput. Chem.* **2004**, *25*, 1157–1174.
- (57) Jakalian, A.; Bush, B. L.; Jack, D. B.; Bayly, C. I. *J. Comput. Chem.* **2000**, *21*, 132–146.
- (58) Jakalian, A.; Jack, D. B.; Bayly, C. I. *J. Comput. Chem.* **2002**, *23*, 1623–1641.
- (59) Darden, T.; York, D.; Petersen, L. *J. Chem. Phys.* **1993**, *98*, 10089.
- (60) Hess, B.; Bekker, H.; Berendsen, H. J. C.; Fraaije, J. G. E. M. *J. Comput. Chem.* **1998**, *18*, 1463–1472.
- (61) Berendsen, H. J. C.; Postma, J. P. M.; van Gunsteren, W. F.; Dinola, A.; Haak, J. R. *J. Chem. Phys.* **1984**, *81*, 3684.
- (62) Nosé, S. *J. Chem. Phys.* **1984**, *81*, 511–519.
- (63) Parrinello, M.; Rahman, A. *J. Appl. Phys.* **1981**, *52*, 7182–7190.
- (64) Harris, C. R. et al. *Nature* **2020**, *585*, 357–362.
- (65) Virtanen, P. et al. *Nat. Meth.* **2020**, *17*, 261–272.
- (66) McKinney, W. Data Structures for Statistical Computing in Python. Proceedings of the 9th Python in Science Conference. 2010; pp 51–56.
- (67) Michaud-Agrawal, N.; Denning, E. J.; Woolf, T. B.; Beckstein, O. *J. Comput. Chem.* **2011**, *32*, 2319–2327.
- (68) Huson, D. H.; Bryant, D. *Mol. Biol. Evol.* **2006**, *23*, 254–267.
- (69) Hunter, J. D. *Comput. Sci. Engineer.* **2007**, *9*, 90–95.
- (70) Williams, T.; Kelley, C.; many others, Gnuplot 4.6: an interactive plotting program. <http://gnuplot.sourceforge.net/>, 2013.

- (71) Ramachandran, P.; Varoquaux, G. *Computing in Science & Engineering* **2011**, *13*, 40–51.
- (72) Humphrey, W.; Dalke, A.; Schulten, K. *J. Mol. Graph.* **1996**, *14*, 33–38.
- (73) Schrödinger, LLC, **2015**,
- (74) Hall, R.; Dixon, T.; Dickson, A. *Front. Mol. Biosci.* **2020**, *7*.
- (75) Sittel, F.; Stock, G. *J. Chem. Theory Comput.* **2016**, *12*, 2426–2435.
- (76) Sittel, F.; Stock, G. *J. Chem. Phys.* **2018**, *149*, 150901.

# Supplementary Information

## Supplementary Figures

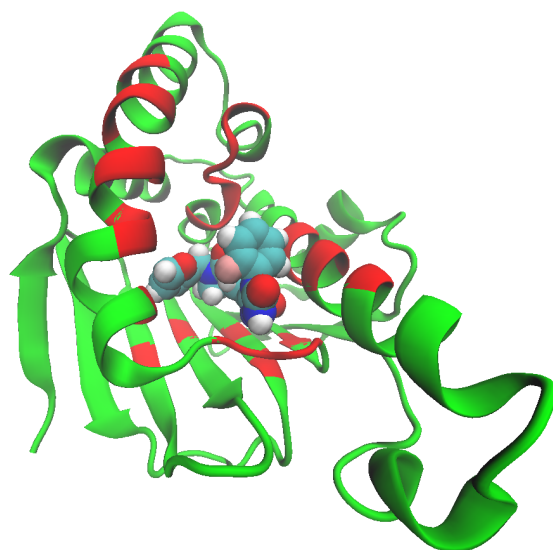


Figure S 1: Selected contacts for conPCA (red): Asn51, Ser52, Asp54, Ala55, Lys58, Asp93, Ile96, Gly97, Met98, Leu103, Leu107, Gly108, Ile110, Ala111, Ser113, Gly114, Ala117, Phe134, Gly135, Val136, Gly137, Phe138, Tyr139, Val150, Trp162, Thr184, Val186.

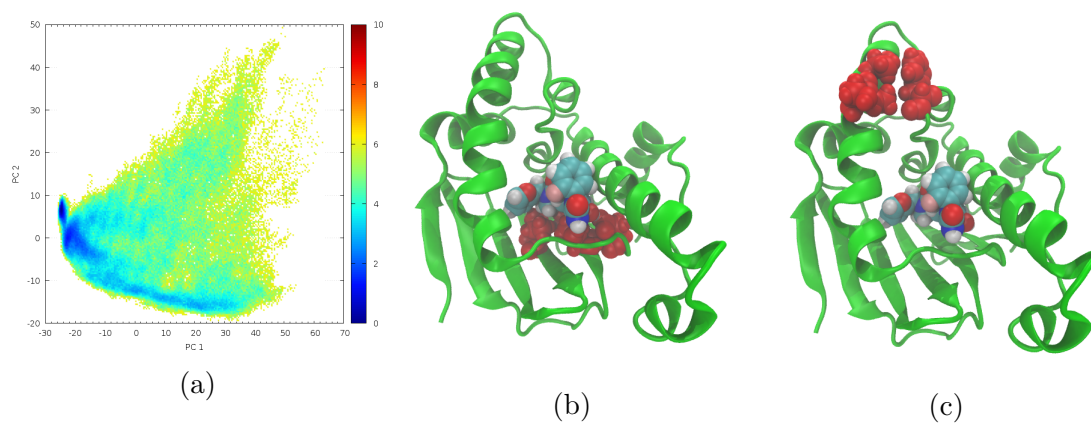


Figure S 2: a: Biased energy diagram  $\Delta\mathcal{G}$  of the first two PCs for ligand **1** (100 trajectories). Coloring represents the value of  $\Delta\mathcal{G}$ . b, c: top residues representing PC1 (a) and PC2 (c) in the respective eigenvector content from Fig. S4.

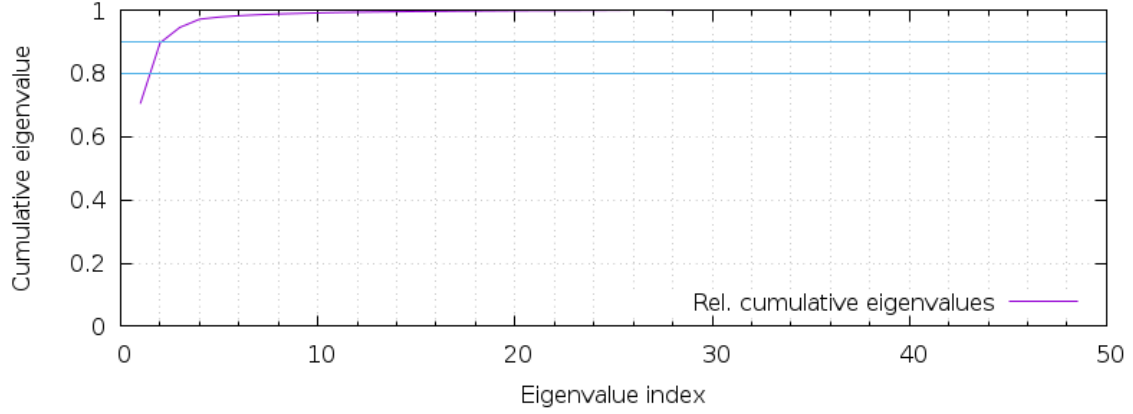
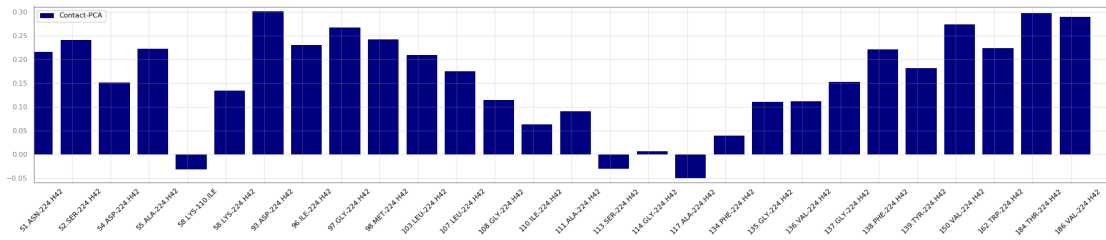
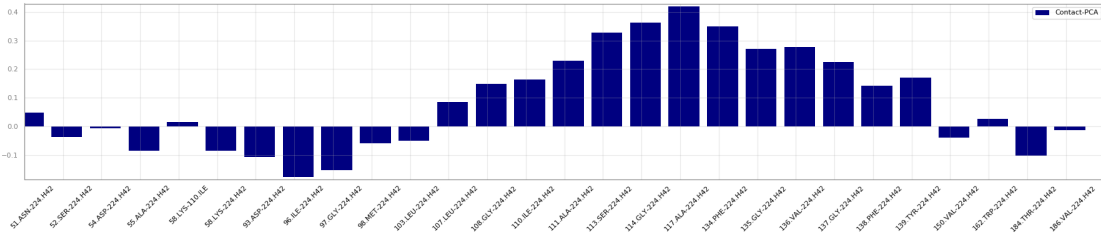


Figure S 3: Cumulative eigenvalues for conPCs.



(a) PC1



(b) PC2

Figure S 4: Contribution of each contact to PCs 1 and 2.

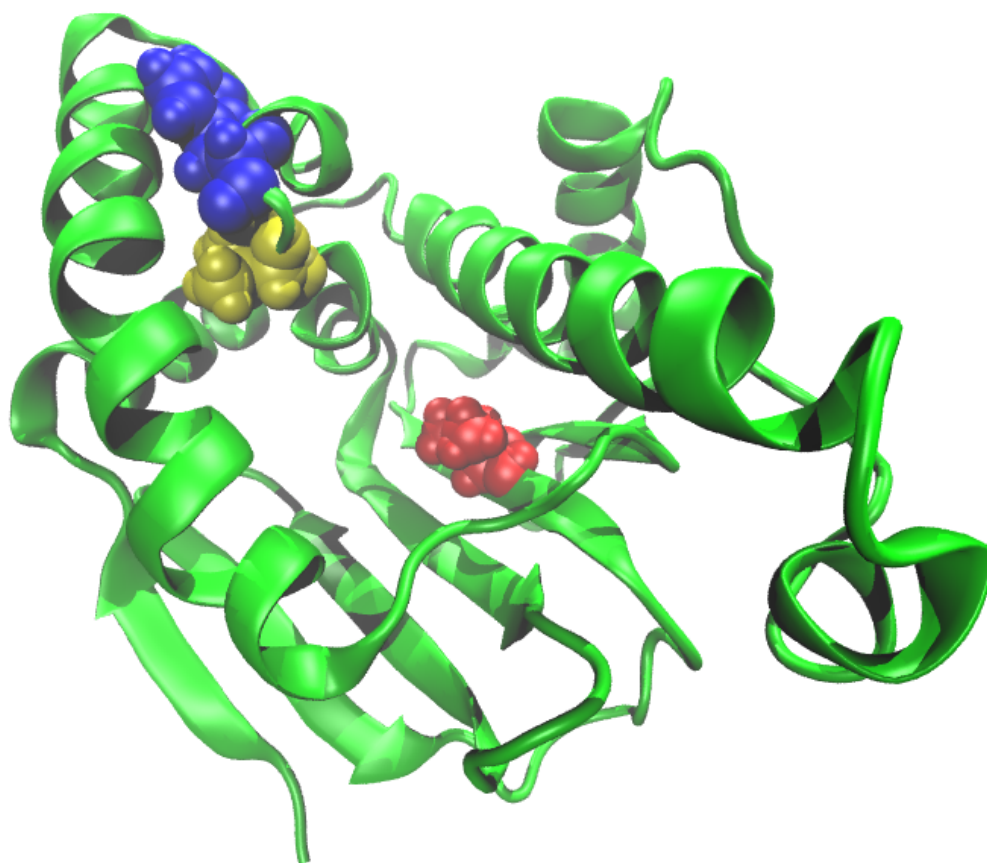


Figure S 5: Machine Learning feature location in compound **1**. Phe134 (blue), Val136 (yellow) and Val186 (red) in the structure of Hsp90. (For clarity the ligand is not shown.)

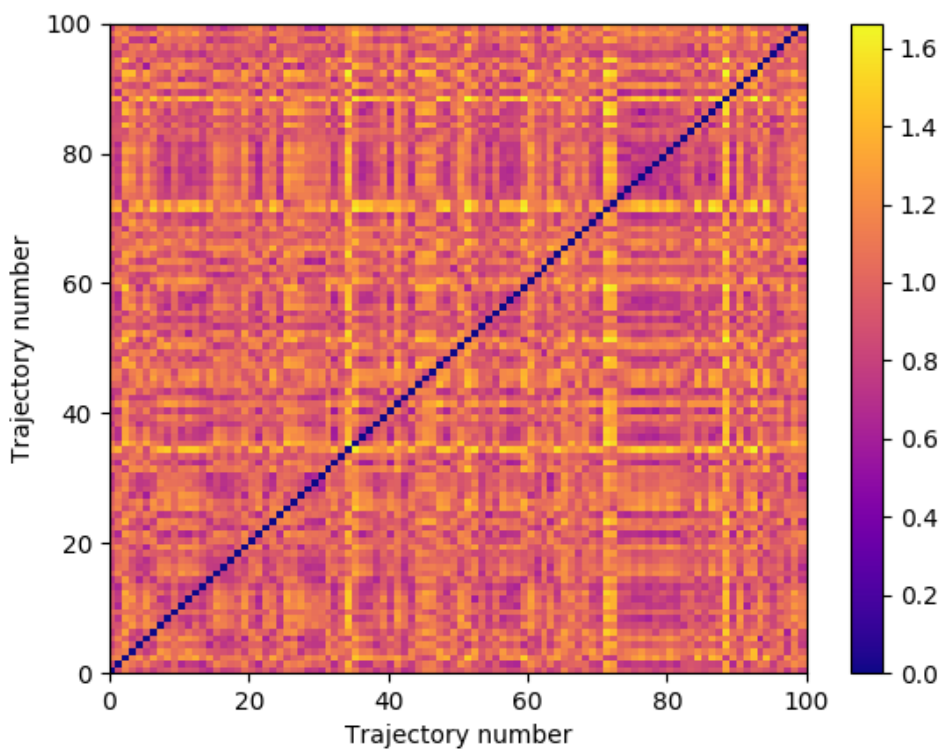


Figure S 6: Representation of distance matrix of 100 clustered **1** trajectories as a color map, for illustrative purposes. Each pixel represents the mean RMSD distance in nm, averaged over time, between the ligand heavy atoms in two trajectories. Lighter colors indicate greater distances.

## Supplementary Tables

Table S 1: ML importance values for compound **1** first five contacts.

Amino acid contact	Importance value
Val186	0.31
Val136	0.29
Phe134	0.26
Ala117	0.04
Thr184	0.02

Table S 2: Statistics for **3** and **4** pathway separation.

Ligand/path	No. of trajectories
<b>3</b>	100
<b>4</b> (all)	531
<b>4</b> (no H-bond)	284
<b>4</b> (with H-bond)	247